Supporting Information

Magnetism of new metastable cobalt-nitride compounds

Balamurugan Balasubramanian,*[a,b] Xin Zhao,[c,d] Shah R. Valloppilly,[a] Sumit Beniwal,[a,b] Ralph Skomski,[a,b] Anandakumar Sarella,[a] Yunlong Jin,[a,b] Xingzhong Li,[a] Xiaoshan Xu,[a,b] Huibo Cao,[e] Haohan Wang,[a,b] Axel Enders,[f] Cai-Zhuang Wang,[c,d] Kai-Ming Ho,[c,d] and David J. Sellmyer*[a,b]

[a] *Nebraska Center for Materials and Nanoscience, University of Nebraska, Lincoln, NE-68588, USA.*

[b] *Department of Physics and Astronomy, University of Nebraska, Lincoln, NE-68588, USA.*

[c] *Ames Laboratory, US Department of Energy, Ames, Iowa 50011, USA.*

[d] *Department of Physics and Astronomy, Iowa State University, Ames, Iowa 50011, USA.*

[e] *Quantum Condensed Matter Division, Oak Ridge National Lab, Oak Ridge, TN 37831, USA.*

[f] *Physikalisches Institut, Universität Bayreuth, 95440 Bayreuth, Germany*

Corresponding authors: bbalasubramanian2@unl.edu;dsellmyer@unl.edu

Supporting Information S1: Methods

Experimental Section

Sample preparation. The Co_3N nanoparticles were produced using an inert-gas plasma condensation-type cluster-deposition method described elsewhere.[1] The experimental setup consists of two chambers, one for cluster formation and the other for deposition as schematically shown in Fig. S1A. The cluster-formation chamber has a direct current (DC) magnetron plasma-sputtering discharge with a water-cooled gas-aggregation tube, where Co is sputtered using a mixture of argon (Ar) and helium (He) as the sputtering gas. The flow rates of Ar and He used for sputtering are 400 and 100 SCCM (SCCM denotes standard cubic centimeter per minute), respectively. A high dc power $P_{dc} \approx 200$ W was used for sputtering.

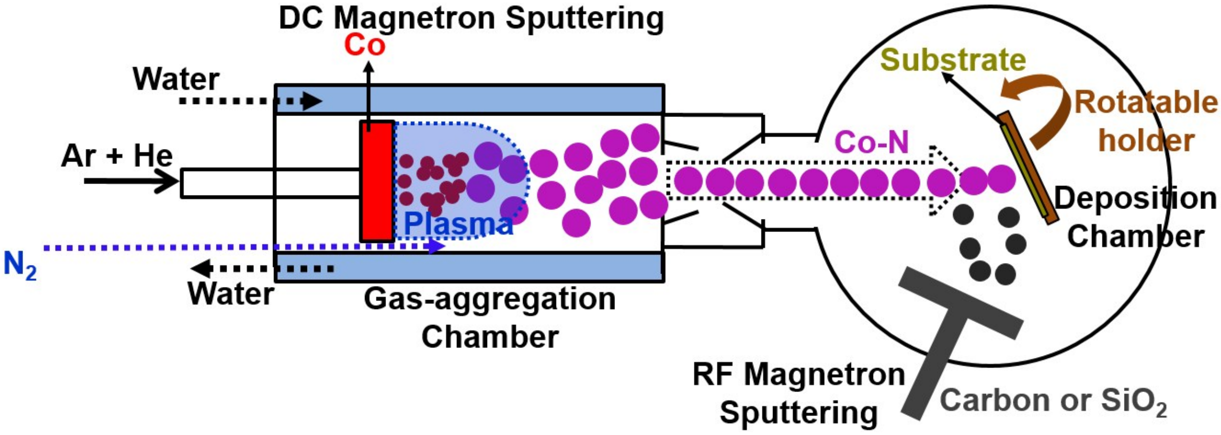

Figure S1A. Fabrication of Co_3N nanoparticles. A schematic of the cluster-deposition method.

During the particle formation, N_2 was introduced into the plasma region so that the sputtered Co atoms react with nitrogen ions in the plasma to form Co-N nanoparticles. The composition and crystal structure of the nanoparticles was varied by controlling the flow rate of N_2. While a N_2 flow rate of about 25 SCCM was used for forming the $CdMg_3$-type hexagonal $Co_{3.3}N$ nanoparticles, the rhombohedral $Co_{2.8}N$ structure was fabricated at a flow rate of 30 SCCM. For the deposition of cubic CoN nanoparticles, a high flow rate of about 100 SCCM was used. The nanoparticles were extracted as a collimated beam moving towards the deposition chamber for the deposition on substrates kept at room temperature. For easy-axis alignment, the nanoparticles were aligned by applying a magnetic field $B_x \approx 0.5$ T (5 kG) using a set of permanent magnets before deposition on substrates (For schematic, see Fig. S4A in the Supporting Information S4).

Characterization. Nanoparticles were deposited on carbon coated copper grids with low coverage densities to measure the average particle size and size distribution using a FEI Tecnai Osiris (Scanning) transmission-electron microscope. Thin-film assemblies of dense-packed nanoparticles were fabricated on single-crystalline Si (111) substrates for other characterizations using the Quantum Design Superconducting Quantum Interference Device (SQUID), Physical Property Measurement System (PPMS), and x-ray diffraction (XRD, Rigaku Smart Lab Diffractometer, where a Cu K_α wavelength of about 1.54 Å is used). The neutron diffraction was performed using the four-circle neutron diffractometer HB-3A at the High Flux Isotope Reactor (HFIR) at the Oak Ridge National Laboratory (ORNL). The high flux neutrons with the wavelength of 1.546 Å were used. The nanoparticles and thin-film samples were capped with a carbon layer immediately after deposition using a radio-frequency magnetron sputtering gun employed in the deposition chamber. X-ray photoemission spectroscopy (XPS) measurements were obtained using an Omicron non-monochromatized Al $K\alpha$ x-ray source, with a photon energy of 1486.6 eV, and a SPECS PHOIBOS 150 energy analyzer. For XPS measurements, a capping layer was not used to cover the nanoparticle film, but the surface contamination caused by the exposure to air was removed by an *in situ* sputtering using argon ions with an energy of 1.5 keV and a current of 3 μA, prior to measurement.

Density functional theory. First-principles calculations were performed using spin-polarized density functional theory (DFT). Generalized-gradient approximation (GGA) implemented in the VASP code[2] was used in the form of PBE.[3] A plane-wave basis was used with kinetic energy cutoff of 520 eV. The Monkhorst-Pack's scheme was adopted for Brillouin zone sampling with a k-point grid resolution of 2π × 0.03 Å^{-1} being used in the structure refinements.[4] The ionic relaxations were stopped when the forces on every atom was smaller than 0.01 eV/Å. The magnetization of the new structures, shown in Table 1, were also calculated using VASP.

Table 1. Calculated Co_3N structures, formation energy (ΔH) at equilibrium or standard conditions, and saturation magnetization M_s. The calculations for formation energy of Co_3N were made using hcp Co and N_2 as references by ΔH (Co_3N) = [E(Co_3N) – 0.5E(N_2) – 3E(Co)]/4.

Structure No	Crystal Structure	Space group	ΔH (meV/atom)	M_s (kA/m or emu/cm^3)
Co_3N-1	Rhombohedral	$R\bar{3}c$ (hexagonal axes)	+71.0	662
Co_3N-2	Orthorhombic	C 2/m 2/c 21/m	+106.1	537
Co_3N-3	Orthorhombic	C 2/m 2/c 21/m	+116.4	959
Co_3N-4	Orthorhombic	C 2/m 2/m 2/m	+116.5	973
Co_3N-5	Orthorhombic	C 1 m 1	+128.3	561
Co_3N-6	Orthorhombic	C 2/m 2/c 21/m	+141.4	649
Co_3N-7	Orthorhombic	I 2/m 2/m 2/m	+141.6	766
Co_3N-8	Hexagonal	P63/mmc	+964.1	1198

Additional electron Diffraction patterns.

Figure S1B shows the electron diffraction pattern for the hexagonal Co_3N nanoparticles. In order to see the diffraction spots corresponding to the (100) reflection of the $CdMg_3$-type structure, the intensity of the incident electron beam is decreased by adjusting the beam-stopper. As shown in Fig. S1B, a few diffraction spots corresponding to (100) reflection of the hexagonal $CdMg_3$-type structure is clearly seen.

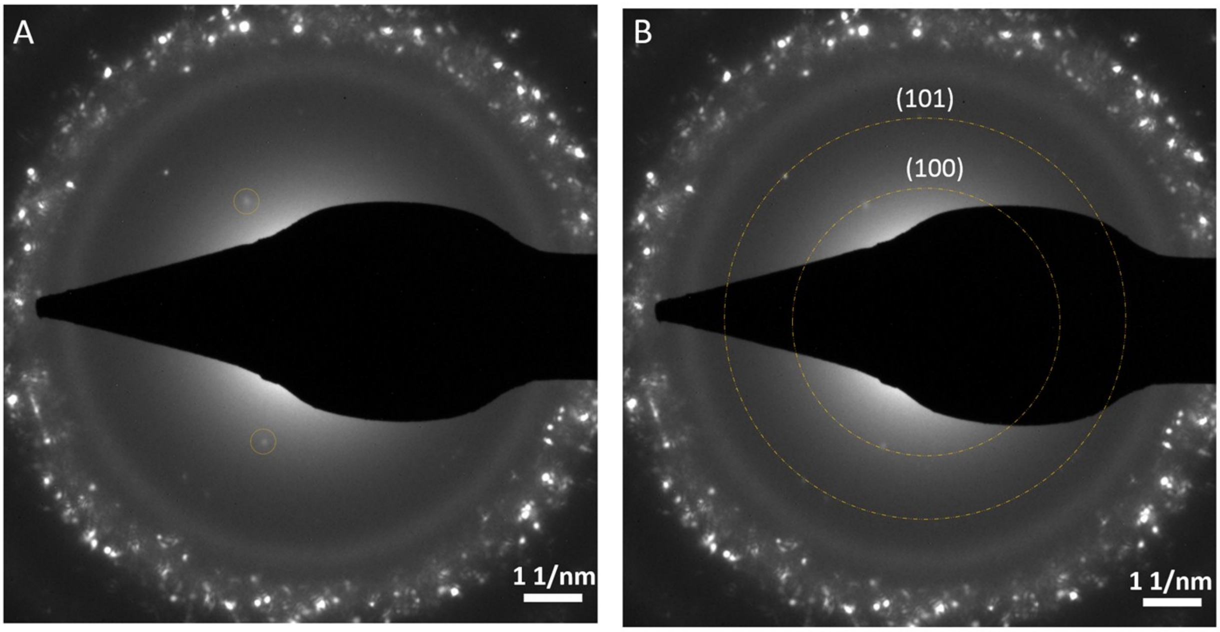

Fig. S1B. Hexagonal Co$_{3.3}$N nanoparticles. (A) A selected area diffraction pattern (SAED)**. (B)** The SAED pattern is indexed with the (101) and (100) reflections of the CdMg$_3$-type hexagonal structure.

Supporting Information S2: XPS analysis for the Co$_3$N nanoparticles

The core-level Co 2p and N 1s spectra measured for the hexagonal- and rhombohedral-type Co$_3$N nanoparticles are shown in Figs. S2-1A and S2-1B and Figs. S2-1C and S2-1D, respectively. Note that the compositional analysis using XPS is a straightforward approach and we have used the areas of whole Co 2p$_{3/2}$ and N 1s peaks and the corresponding relative sensitivities factors to determine the Co/N atomic ratio in the nanoparticles. The Co/N atomic ratios determined for the hexagonal- and rhombohedral-type Co$_3$N nanoparticles are about 3.3 and 2.8, respectively. In order to understand the physical significance of the spectral features, we also carried out peak fit analysis for the XPS spectra of the hexagonal- and rhombohedral-type nanoparticles as described below.

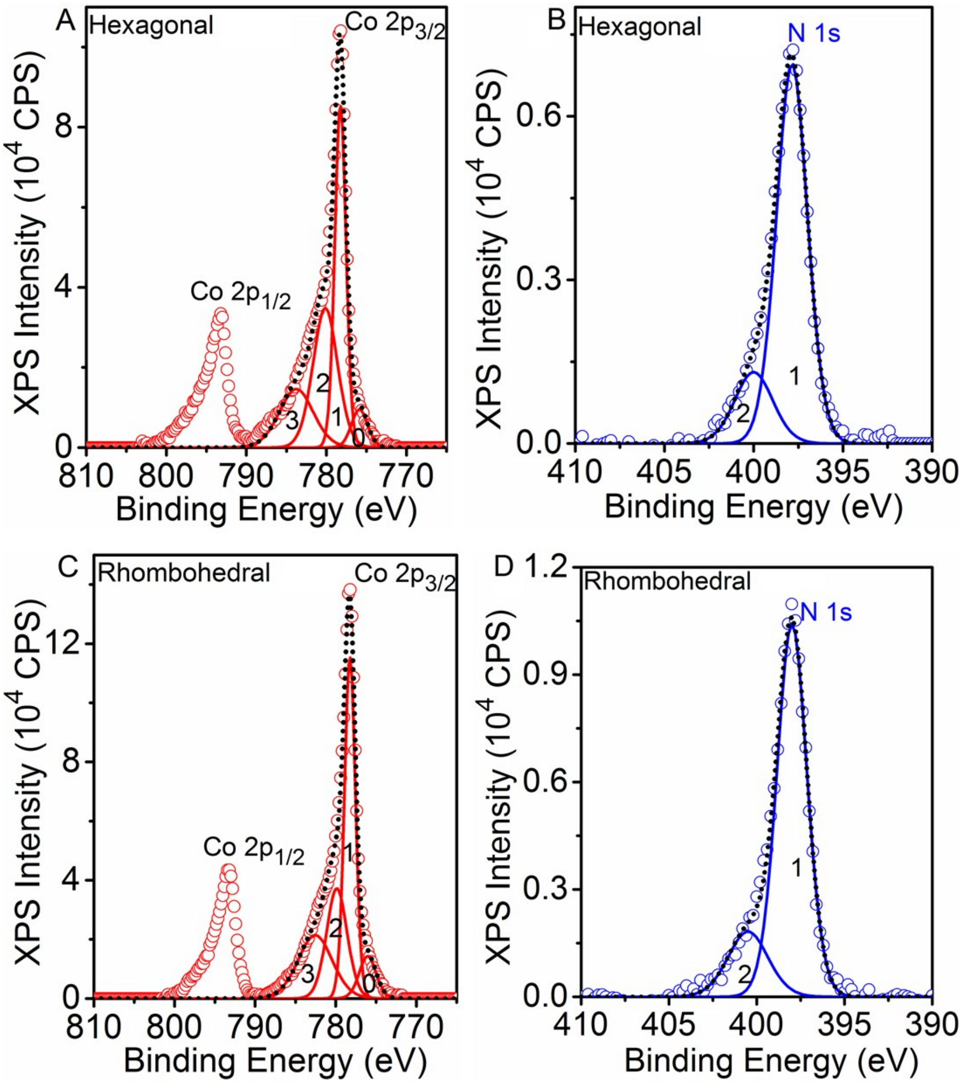

Figure S2-1. Experimental Co 2p and N 1s core-level XPS spectra (open circles). (A), (B) Hexagonal-type Co$_{3.3}$N nanoparticles. (C), (D) Rhombohedral-type Co$_{2.8}$N nanoparticles. The experimental Co 2p$_{3/2}$ peak is fitted with a main peak (peak 1) followed by two plasmon-loss peaks at higher binding energy side (peaks 2 and 3, respetively). A minor contribution from Co LMM Auger transitions to the Co2p$_{3/2}$ peak is also fitted as peak 0. Similarly, the experimental N1s peak is fitted with a main peak (peak 1) along with a compartively weak peak (peak 2), possibly corrsponding to a plasmon absorption. Note that the solid-line curves are fitted peaks for Co2p$_{3/2}$ and N 1s peaks corresponding to various spectral contributions. The dotted curves are the resultant spectra of the fitted peaks.

Generally Co 2p spectrum has a complex structure and consists of doublet peaks Co2p$_{3/2}$ and Co 2p$_{1/2}$ due to spin-orbit splitting. In addition, the Co 2p$_{3/2}$ and Co 2p$_{1/2}$ peaks are also asymmetric due to the presence of plasmon loss features and/or satellite peaks depending on the chemical environment.[5,6] In the case of metallic samples, the Co 2p$_{3/2}$ XPS peak is always composed of a main peak followed by two plasmon-loss peaks at higher binding energy side, which correspond to surface and bulk plasmons, respectively.[5-7] Note that the Co $2p_{3/2}$ peak overlaps with a portion of minor contribution from Co LMM Auger transitions at around 776 eV and thus the lower-energy tail of the $Co2p_{3/2}$ peak is also asymmetric. By taking all above considerations into account, Co $2p_{3/2}$ XPS peaks of the hexagonal- and rhombohedral-type Co_3N nanoparticles are mainly fitted into a main peak (peak 1) and two plasmon-loss peaks (peak 2 and peak 3 corresponding to surface and bulk plasmons, respectively) as shown in Fig. S2-1A and Fig. S2-1C, respectively. A weak peak (peak 0) is also added to compensate for the asymmetry caused by the overlapping minor Co LMM Auger transitions (peak 0). The presence of pure Co is not clearly distinguishable in the Co2p XPS spectrum of the hexagonal-type nanoparticles because of its low content (about 3 vol. %). Thus, we have excluded the peaks corresponding to pure Co in the fitting and quantification analysis for hexagonal-type $Co_{3.3}N$.

The core-level N 1s spectra are also slightly asymmetric at the higher binding-energy side as shown in Fig. S2-1B and S2-1D, respectively. Note that N 1s spectrum of iron and cobalt nitrides also has been shown to be slightly asymmetric at the higher binding-energy tail.[8,9] Although the origin of this feature is not known, it can be possibly due to the presence of a peak corresponding to plasmon absorption, seen in other metallic nitrides.[10] Thus, we have fitted the N 1s spectra of the hexagonal- and rhombohedral-type nanoparticles with an intense main peak along with a minor peak as shown in Fig. S2-1B and S2-1D, respectively. The peak positions of N 1s spectra for the hexagonal- and rhombohedral-type nanoparticles are about 397.8 and 398.0 eV, respectively and these values are in the range of binding energy values reported for metal nitrides.[9,11] The position of Co $2p_{3/2}$ XPS peaks are also slightly higher for the hexagonal $Co_{3.3}N$ (778.3 eV) and rhombohedral $Co_{2.8}N$ nanoparticles (778. 2 eV), as compared to the standard value of Co metal (777.9 eV).[9, 13]

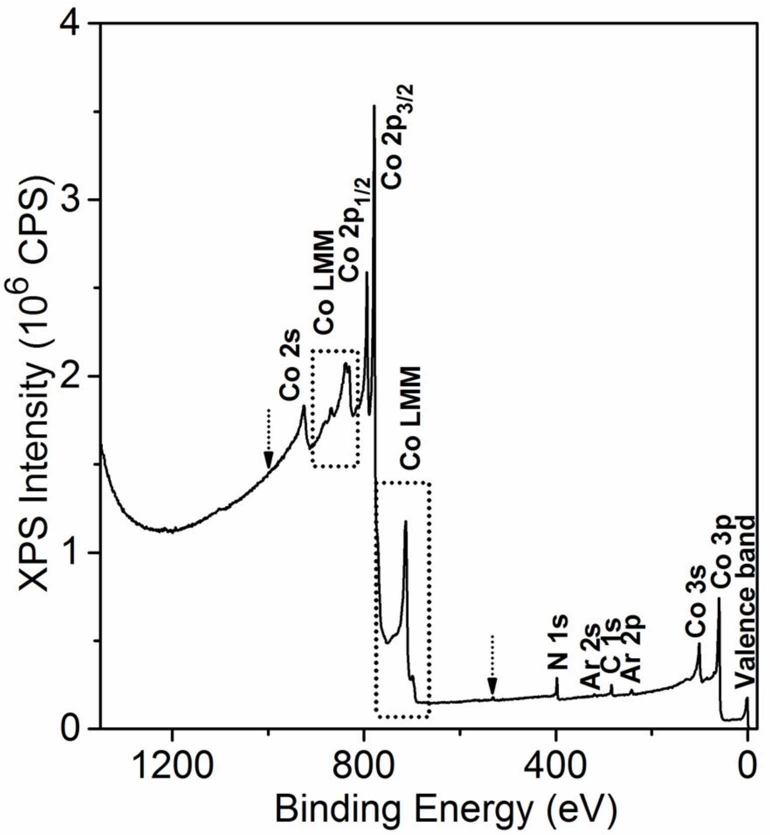

Fig. S2-2 XPS survey spectrum of the hexagonal cobalt nitride nanoparticles. The arrows at around 531.6 eV and 999 eV are placed to show a substantialy weak presence of O 1s XPS peak and an absence of O KLL Auger transitions, respectively.

Note that the nanoparticles/films used for TEM and XRD measurements are immediately capped with about a 1-3 nm thick carbon layer using a RF sputtering gun employed in the deposition chamber to prevent oxidation upon exposure to air. Figure S2-2 shows a wide scan (survey) spectrum measured for the hexagonal cobalt nitride nanoparticles using monochromatic *Al Kα* x-ray with an energy of 1486.6 eV by *Thermo Scientific K-alpha*$^+$ XPS. In addition to weak Ar and C XPS peaks, the survey spectrum shows significantly intense XPS peaks and/or Auger transitions corresponding to only Co and N and reveals a high purity in the sample. It is clearly seen from Fig. S2-2 that O 1s is substantially weak (indicated by an arrow at about 531.6 eV) and the characteristic O KLL Auger transitions is completely absent as indicated by an arrow around 999 eV. The weak O1s peak only yields about 1 at. % of oxygen in the sample, and its peak position is about 531.6 eV, which is higher than that of the O 1s XPS peak corresponding to CoO (530.0 eV).[12] This result indicates that the substantially weak O 1s XPS peak may be due to adsorbed oxygen molecules (possibly from moisture). In addition, the absence of characteristic satellite peaks of CoO in the Co 2p XPS spectra and (*hkl*) reflections of the CoO structure in the XRD and SAED patterns also rules out the possible presence CoO phase.

Supporting Information S3: Phase decomposition of the hexagonal Co$_{3.3}$N nanoparticles

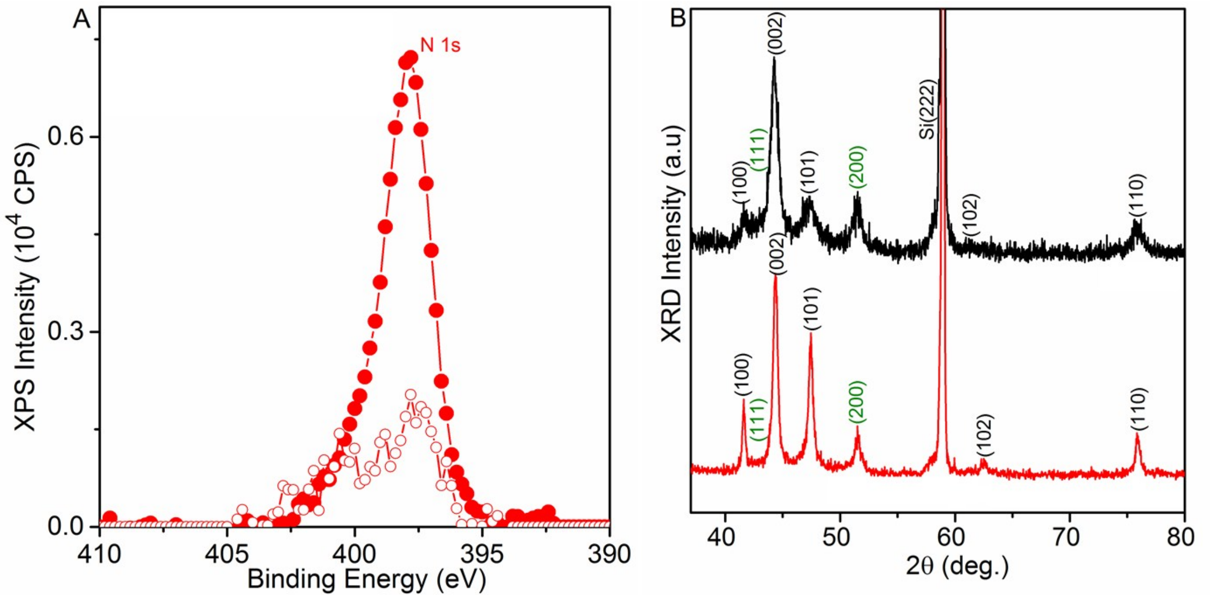

Figure S3. Phase decomposition of the hexagonal-type Co$_{3.3}$N nanoparticles. (A) The N 1s core-level XPS spectra for the as-deposited Co$_{3.3}$N nanoparticles (solid circles) and annealed nanoparticles at 850 K for 10 min (open circles). The N 1s XPS peak becomes very weak and noisy with substantially low intensity, indicating a nearly complete nitrogen loss from the sample upon annealing at 850 K. (B) XRD pattern of the annealed nanoparticles (red curve) are compared with that of the pure Co nanoparticles (black curve). This result shows that the Co$_{3.3}$N nanoparticles transforms into pure Co phase after annealing at 850 K, which exhibit XRD pattern similar to that of pure Co nanoparticles. The XRD peaks corresponding to hcp Co and fcc Co are indexed in black and green fonts, respectively.

Supporting Information S4: Easy-axis alignment of the hexagonal $Co_{3.3}N$ nanoparticles

Experimental process. The easy-axis of the $Co_{3.3}N$ nanoparticles was aligned prior to deposition using a magnetic field $B_x = \mu_0 H_x$ 0.5 T (5 kG), which was applied along the *x*-direction, parallel to the substrate as shown in Fig. S4A. The *x*-axis therefore expected to be the easy magnetization direction, whereas both the *y*- and *z*-directions are hard directions.

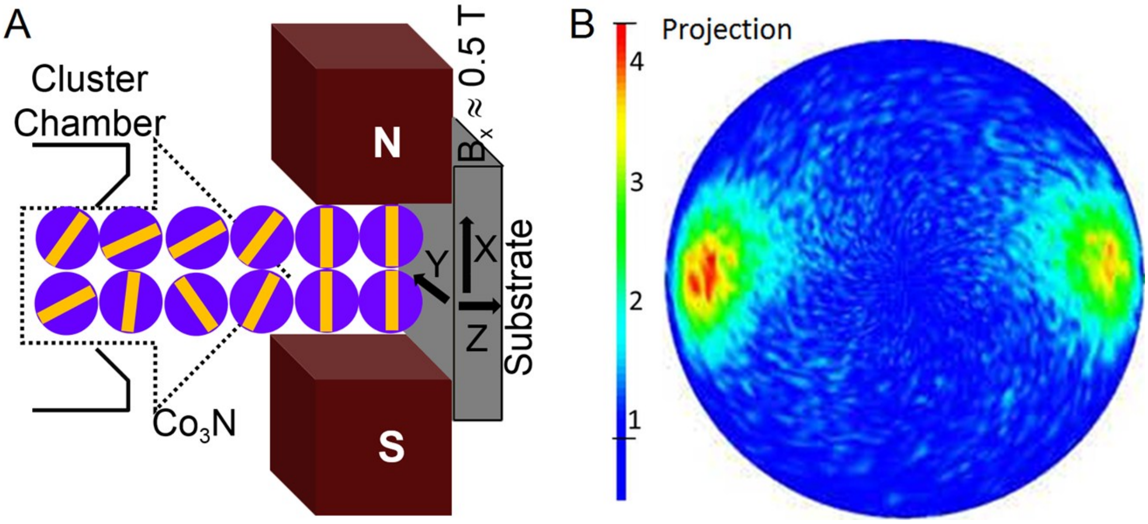

Figure S4. Easy-axis aligned hexagonal-type $Co_{3.3}N$ nanoparticles. (A) Schematic of easy-axis alignment by applying a magnetic field ($B_x \approx \mu_0 H_x = 0.5$ T or 5 kG) along the x-axis using a pair of permanent magnets (N-S). ((B) In-plane pole-figure of the (002) peak.

Pole-figure analysis of the (002) peak. A detailed picture of the magnetic alignment of the nanoparticles and its corroborative evidence linked to the crystallographic c-axis can understood from the pole-figure analysis of the (002) peak. The in-plane polefigure of the (002) peak for the nanoparticles deposited in an applied magnetic field of ~ 0.5 T along the x-axis is shown in Fig. S4B. Here, a 2D plot of a hemispherical scattered intensity distribution of (002) peak is presented and it clearly shows two high intensity spots on the opposite ends of the pole plot. The orientation distribution of the (002) planes is rather narrow along the direction that coincides with the direction of applied field, x. Note that the center of the pole-plot represents the surface normal (α = 90°) while its variation from center along the radius towards the circumference (α = 0°) represents the gradual variation of tilt angle of the diffraction plane. A line plot analysis shows that the intensity maxima is centered around (α = 15 ± 5°) from the Si substrate plane with a full width at half maximum (FWHM) of about 20°. This observation that the intensity maxima does not exactly coincide with α = 0° can be attributed to some slight misalignment between the effective magnetic field and the substrate orientations. Nevertheless, the results prove that the {002} is achieved predominantly along the direction of H_x in the film plane (Fig. S4B).

Supporting Information S5: Magnetic properties and phase stability of the rhombohedral $Co_{2.8}N$ nanoparticles

Unlike the hexagonal-type $Co_{3.3}N$ nanoparticles, the magnetization of the rhombohedral-type nanoparticles changes significantly upon varying the measurement temperatures from 10 K to 300 K as shown in the temperature-dependent hysteresis loops (Fig. S5A). The rhombohedral $Co_{2.8}N$ nanoparticles exhibit a high $B_c = \mu_0 H_c = 0.6$ T (6.0 kG) at 10 K and maintain a decent coercivity up to 150 K ($B_c = 0.03$ T at 150 K). This coercive behavior can be attributed to a high magnetocrystalline anisotropy.

We have estimated K_1 and M_s for the rhombohedral-type $Co_{3.3}N$ nanoparticles by fitting the 10 K-magnetization curve in the high-field region (3.0 to 7.0 T) using the law-of-approach to saturation method.[14] Fig. S5B show the experimental and fitted magnetization curves. This analysis yield $K_1 = 1.04$ MJ/m^3 (10.4 Mergs/cm^3), and $M_s = 580$ kA/m (580 emu/cm^3), which is in good agreement with those obtained using the DFT calculations (M_s = 662 kA/m).

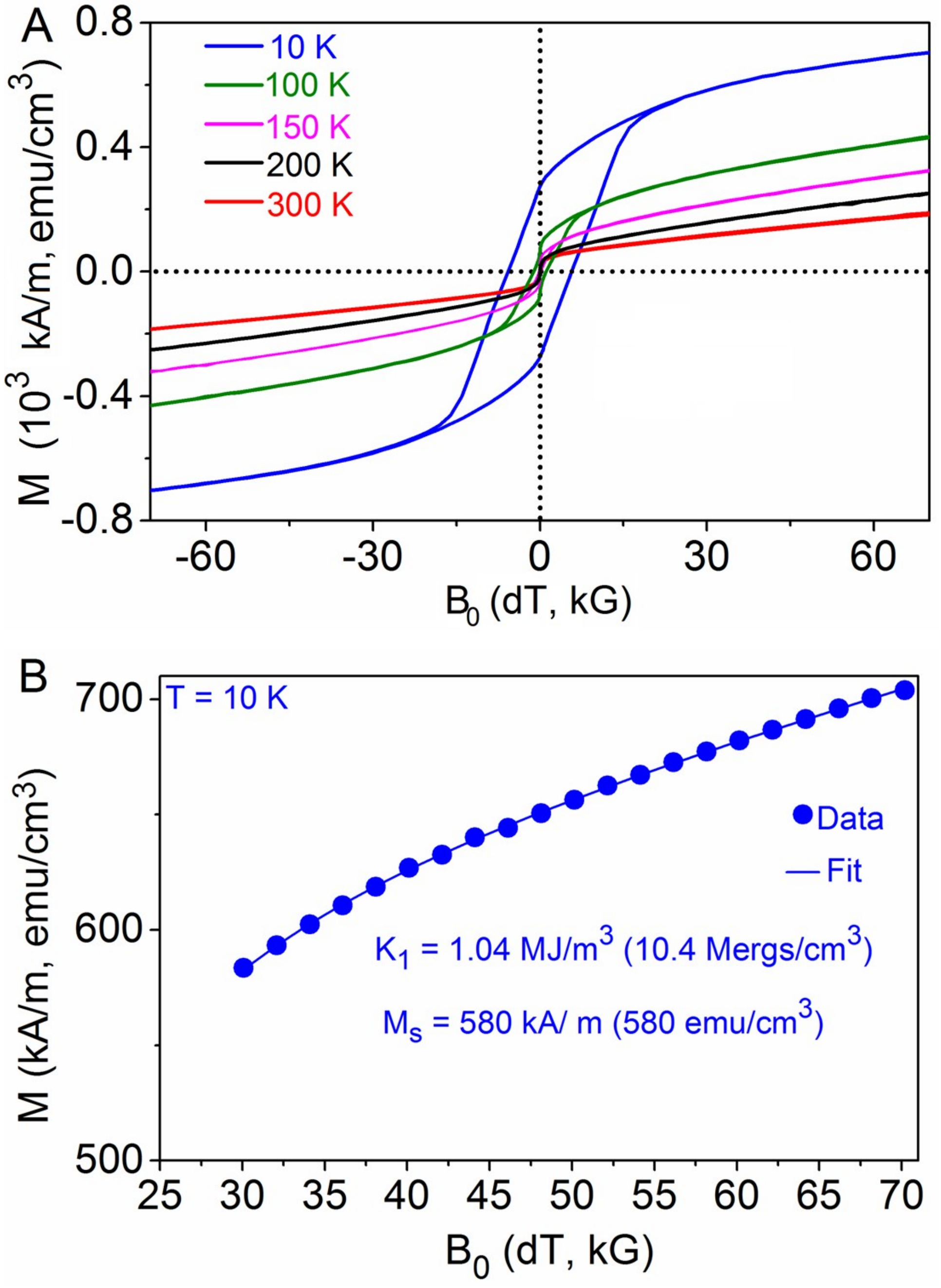

Figure S5. Magnetic properties of the rhombohedral-type $Co_{2.8}N$ nanoparticles. (A) Temperature-dependent hysteresis loops. (B) Analysis using the law-of-approach to saturation: To estimate the magnetic anisotropy constant K_1 and saturation magnetization M_s for the rhombohedral-type $Co_{2.8}N$ nanoparticles by following the law-of-approach to saturation,[14] the magnetization near saturation (M_s) in the field range of 3.0 – 7.0 T for the in-plane magnetization curve is fitted using the equation $M = M_s (1 - A/H^2) + \chi H$. Here χ is the high-field susceptibility and the constant A depends on the anisotropy constant K_1 as given by $A = \frac{4}{15} \frac{K12}{Ms2}$. This analysis yields $K_1 \approx 1.04$ MJ/m^3 (10.4 Mergs/cm^3), and $M_s = 580$ kA/m (580 emu/cm^3), which corresponds to $J_s = 0.73$ T (7.3 kG).

In order to see the magnetic transition and decomposition of the rhombohedral $Co_{2.8}N$ phase, a temperature-dependent magnetization curve is also measured in the range of 300 K – 900 K as shown in Fig. S6. The magnified *M-T* curve of the heating cycle in the range of 300 K – 600 K is also shown as an inset in Fig. S6. As observed in the case of hexagonal-type nanoparticles, the magnetization of the rhombohedral nanoparticles increases rapidly above 605 K and approach to a saturation at about 710 K. This temperature-dependent magnetic behavior can be attributed to the conversion of Co_3N phase to pure Co,[15] which is also supported by XRD and XPS results as shown in Fig. S7.

Note that the *M-T* curve of the hexagonal-type Co_3N nanoparticles does not show significant changes in the magnetization values in the temperature range of 300 K – 500 K. On the other hand, the magnetization of the rhombohedral nanoparticles decreases abruptly at above 300 K and reaches almost near to zero around 500 K (as shown in the inset of Fig. S6). This suggests that the Curie temperature of the rhombohedral $Co_{2.8}N$ phase is in the vicinity of 450 K – 500 K.

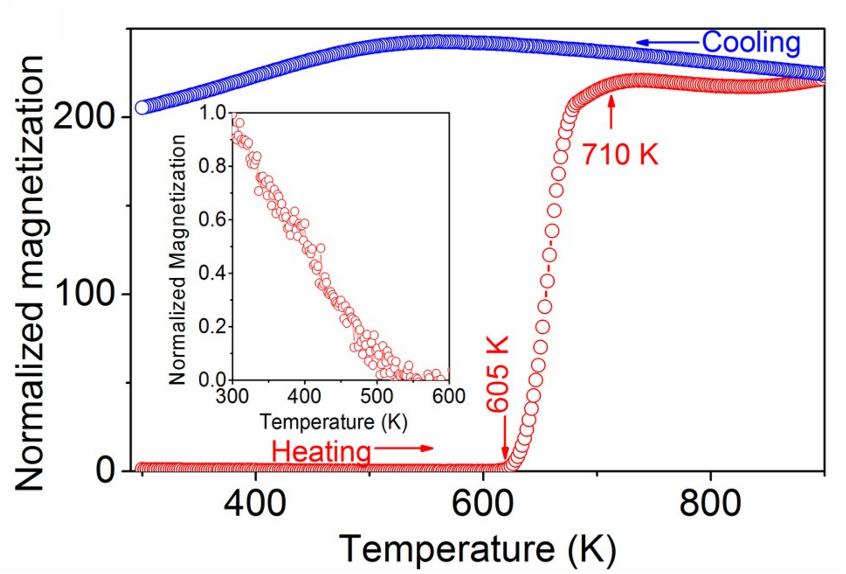

Figure S6. Temperature-dependent magnetization curves for the rhombohedral $Co_{2.8}N$ nanoparticles. The magnetization is normalized with the room-temperature value and the measurement is performed in a magnetic field of 0.5 dT (0.5 kG) during the heating (red curve) and cooling (blue curve). The magnetization curve measured in the temperature range of 300 K – 600 K during the heating cycle is shown as an inset.

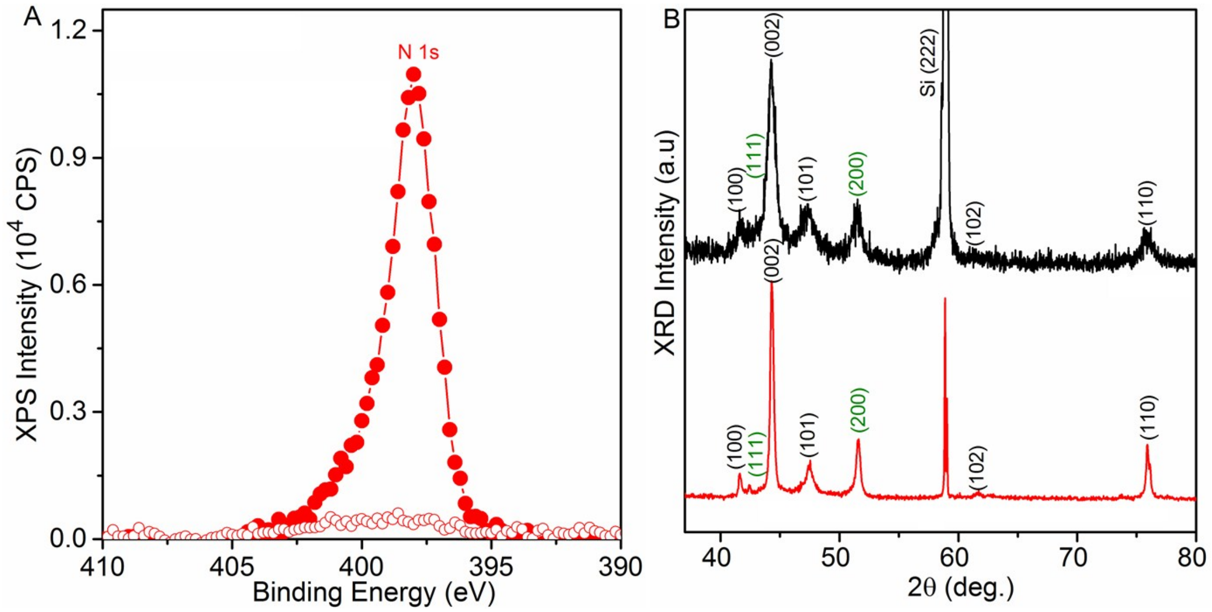

Figure S7. Phase decomposition of the rhombohedral-type $Co_{2.8}N$ nanoparticles. (A) The N 1s core-level XPS spectra for the as-deposited $Co_{2.8}N$ nanoparticles (solid circles) and annealed nanoparticles at 850 K for 10 min (hollow circles). The N 1s XPS peak becomes very weak and noisy with substantially low intensity, indicating a nearly complete nitrogen loss from the sample upon annealing at 850 K. **(B)** XRD pattern of the annealed nanoparticles (red curve) are compared with that of the pure Co nanoparticles (black curve). This result shows that the $Co_{2.8}N$ nanoparticles transforms into pure Co phase after annealing at 850 K, which exhibit XRD pattern similar to that of pure Co nanoparticles. The XRD peaks corresponding to hcp Co and fcc Co are indexed in black and green fonts, respectively.

References

1 B. Balasubramanian, R. Skomski, X. Li, S.R. Valloppilly, J.E. Shield, G.C. Hadjipanayis, D.J. Sellmyer, *Nano Lett.* **2011**, 11, 1747–1752.

2 G. Kresse, J. Furthmuller, *Comput. Mater. Sci.*, **1996**, **6**, 15 – 50 and *Phys. Rev. B* **1996**,54, 11169 – 11186.

3 J.P. Perdew, K. Burke, M. Ernzerhof, *Phys. Rev. Lett.* **1996**, 77, 3865 - 3868.

4 H. J. Monkhorst, J. D. Pack, *Phys. Rev. B* **1976**, 13, 5188-5192.

5 Biesingera, M.C.; Paynec, B.P.; Grosvenord, A.P.; Laua, L.W.M.; Gerson, A.R.; Smart, R.S.C. *Appl. Surf. Sci*. **2011**, 257, 2717–2730.

6 Grosvenor, A.P.; Wik, S.D.; Cavell, R.G.; Mar, A. *Inorg. Chem*. **2005**, 44, 8988 - 8998.

7 Guler, U.; Shalaev, V.M.; Boltasseva, A. *Materials Today* **2015**, 18, 227-237.

8 Lin, Y.- C.; Hong, J.-Y.; Yen, C.-N.; Tong, S.-.Y.; Tung, M.-J.; Shiu, H.-W.; Chen, C.-H.; Lin, M.-T. *Jap. J. App. Phys.* **2015**, 54, 033002.

9 De La Cruz, W.; Contreras, O.; Soto, G.; Perez-Tijerina, E. *Revista Mexicana De Fisica*, **2006**, 52, 409-412.

10 http://xpssimplified.com/elements/nitrogen.php; Access date: 12/20/2017

11 a) Zhong, X.; Liu, L.; Jiang, Y.; Wang, X.; Wang, L.; Zhuang, G.; Li, X.; Mei, D.; Wang, J.-G.; Su, D.S. *ChemCatChem*. **2015**, **7**, 1826 – 1832. b) Vogt, K.W.; Naugher, L.A.; Kohl, P.A. *Thin Solid Films* **1995**, 256, 106 - 115.

12 M. Hassel and H.-J. Freund, *Surface Science Spectra*, **1998**, 27 273-278.

13 Wagner, C. D.; Riggs, W. M.; Davis, L. E.; Moulder J. F.; Mullenberg, G. E. *Handbook of X-ray Photoelectron Spectroscopy*, (Perkin-Elmer Corp., Eden Prairie, 1979), p-78.

14 Hadjipanayis, G.C.; Sellmyer, D.J.; Brandt, B. *Phys. Rev. B* **1981**, 23, 3349 - 3354.

15 Lourenco, M.B.; Carvalho, M.D.; Fonseca, P.; Gasche, T.; Evans, G.; Godinho, M. *J. Alloys. Comp*. **2014**, 612, 176 - 182.